Defect self-assembly of metal-organic framework triggers ferroptosis to overcome resistance

Haibao Peng [a,b,c], Xingcai Zhang [e], Peng Yang [f], Jiaxu Zhao [a], Wei Zhang [a], Nianping Feng [c,***], Wuli Yang [b,**], Jing Tang [d,*]

[a] *Institute for Translational Brain Research, Fudan University, Shanghai, 200032, China*
[b] *State Key Laboratory of Molecular Engineering of Polymers, Department of Macromolecular Science, Fudan University, Shanghai, 200438, China*
[c] *Department of Pharmaceutical Sciences, Shanghai University of Traditional Chinese Medicine, Shanghai, 201203, China*
[d] *Department of Materials Science and Engineering, Stanford University, Stanford, CA, 94305, United States*
[e] *School of Engineering, Massachusetts Institute of Technology, Cambridge, MA, 02139, United States*
[f] *Engineering Research Center of Molecular- and Neuro-imaging of Ministry of Education, School of Life Science and Technology, Xidian University, 710126, China*

ARTICLE INFO

ABSTRACT

The emergence of multidrug treatment resistance presents a hurdle for the successful chemotherapy of tumours. Ferroptosis, resulting from the iron-dependent accumulation of lipid peroxides, has the potential to reverse multidrug resistance. However, simultaneous delivery of the iron sources, ferroptosis inducers, drugs, and enhanced circulation carriers within matrices remains a significant challenge. Herein, we designed and fabricated a defect self-assembly of metal-organic framework (MOF)-red blood cell (RBC) membrane-camouflaged multi-drug-delivery nanoplatform for combined ferroptosis-apoptosis treatment of multidrug-resistant cancer. Ferroptosis and chemotherapeutic drugs are embedded in the centre of the iron (III)-based MOF at defect sites by coordination with metal clusters during a one-pot solvothermal synthesis process. The RBC membrane could camouflage the nanoplatform for longer circulation. Our results demonstrate that this defect self-assembly-enabled MOF-membrane-camouflaged nanoplatform could deplete the glutathione, amplify the reactive oxidative species oxidative stress, and enable remarkable anticancer properties. Our work provides an alternative strategy for overcoming multidrug resistance, which could regulate the fluidity and permeability of the cell membrane by ferroptosis to downregulate of *P*-glycoprotein protein expression by ferroptosis. This defect self-assembly-enabled MOF-membrane-camouflaged multi-drug-delivery nanoplatform has great therapeutic potential.

1. Introduction

Cancer is the most malignant disease and the second leading cause of mortality worldwide [1]. There is a strong need to explore high-efficiency therapeutic approaches against solid malignancy [2]. As our understanding of nanomedicine deepens, this therapeutic strategy exhibits an excellent performance in efficiently delivering therapeutic payloads to the tumour target [3]. Unfortunately, multidrug resistance (MDR) significantly disturbs heavily hampers the therapeutic efficiency, and leads to a failure [4]. MDR can result from the overexpression of the

ATP-binding cassette transporters, e.g., genetic mutations and *P*-glycoprotein (*P*-gp) [5]. Extensive studies of anticancer agents have established paradigms for understanding drug resistance mechanisms. For example, the development of pump inhibitors and cytotoxic agents against drug resistance, targeting the downregulation of MDR genes, evades or exploits efflux by ATP-binding cassette transporters [6]. Recently, several strategies for overcoming MDR have been developed, including the modulation of reactive oxidative species (ROS) stress [7]. The oxidative stress caused by ROS in the tumour microenvironment (TME) is the essential mechanism of their anticancer activity [8]. In

previously reported studies, oxidative stress occurs when overwhelming ROS fails the cellular antioxidant defense system by increasing the ROS level or decreasing the cellular antioxidant capacity [9].

Ferroptosis is an iron-dependent and nonapoptotic form of the cell death process that is ROS-dependent via the Fenton reaction to propagate phospholipid peroxidation of plasma membranes [10,11]. Ferroptosis is triggered upon dysregulation of lipid peroxidation [12]. Glutathione peroxidase 4 (GPX4) and glutathione (GSH) are the key regulators for protecting cells from lipid peroxidation and inhibiting ferroptosis [13]. Inhibition of GPX4 activity can lead to the accumulation of lipid peroxides [14]. Compared to normal cells, cancer cells exhibit a modified intracellular redox state featuring high levels of antioxidants, such as GSH (4~10-fold) [15]. Intracellular ferric iron can downregulate of GSH, while ferrous ions would react with hydrogen peroxide (H_2O_2) through the Fenton reaction, which elevates hydroxyl radical concentrations and promotes ferroptosis therapy [16]. Consequently, increasing the iron pool and depleting GSH have become a promising strategy to initiate ferroptotic cell death. Pseudolaric acid B (PAB) is a natural diterpenoid derived from Cortex Pseudolaricis, that exhibits various bioactivities such as antiangiogenic activity, antimicrobial/antivirus activity and antitumour activity [17,18]. Additionally, PAB was also found to inhibit cancer cell metastasis, circumvent cancer cell multidrug-resistance, and enhance cancer cell sensitivity to radiotherapy [19]. Moreover, PAB depleted intracellular GSH via p53-mediated xCT pathway, and then triggers ferroptosis in glioma cells [20]. However, the underlying molecular mechanism and delivery systems that allow it to overcome the MDR remain largely unexplored, which limits its applications in clinical trials. Therefore, more emphasis should be put on developing strategies for iron sources and ferroptosis drugs within matrices to deplete GSH and to amplify the ROS oxidative stress to kill therapy-resistant cancers [21].

The iron-based materials of the Institute Lavoisier (MIL) family are a subclass of metal-organic frameworks (MOFs) [22]. MOFs enjoy huge prospects in various applications, such as gas storage, sensing, catalysis and drug delivery [23]. The loading capacity of MOF was limited by the hydrophobic and hydrophilic properties of drugs, the drug molecular weight and drug leakage [24]. Recently, engineered defects in MOFs have been widely investigated for nanoscale drug delivery [25].

Thus, a strategy is needed to mitigate drawbacks by formation of a defect loading structure with multi-functional performance. The "perfect" MOFs with deliberate and elegant ligand design have been attracting surging recognition in drug delivery. Nevertheless, defect engineering has arisen as an exciting approach to further tune sorption, catalysis and physical characteristics [26]. Defect engineering in MOFs is a compelling concept for tailoring material properties, and enables the incorporation of multiple drugs by defect-loading [27]. Although conventional practice is commonly used to prepare drugs containing metal-binding units and MOFs for biomedical applications, drug as modulator of MOFs is rarely investigated in recent studies. Currently, simultaneous distribution of multidrug molecules in MOF structures is left as one of the greatest challenges which inspires us to generate a programmable platform as a tandem catalyst for biomedical applications [28–31].

Herein, we developed a MOF-membrane-camouflaged multi-drug-delivery strategy to target oxidative stress and trigger ferroptosis by simultaneously delivering a ferroptosis drug, depleting GSH, and elevating ROS levels. Iron-based MOFs can be developed for cancer therapy based on ferroptosis via the release of their own iron in lysosomes after endocytosis, employing the Fenton reaction to trigger ROS and onset induce lipid peroxidation. The RBC membrane could camouflage the nanoplatform for longer circulation [32]. Our drug delivery nanoplatform applied the defect structure of MOFs to encapsulate multiple drugs to trigger ferroptosis and overcome MDR, which suggests that defect-loading could be an attractive strategy for multidrug delivery. The defect structure allows several types of drugs entrapped within MOFs composed of ferric ions linked by the 1, 4-benzenedicarboxylate linker ligand and further decorated with an erythrocyte membrane. Consequently, an adoptive defect self-assembly (DSA)-enabled nanoplatform has been designed to address resistance in malignant tumours (Fig. 1).

2. Materials and methods

2.1. Materials

Ferric chloride hexahydrate and 1,4-benzenedicarboxylic acid were purchased from Aladdin Co. Ltd. Pseudolaric acid B (PAB), doxorubicin hydrochloride (DOX) and ferrostatin-1 (Fer-1) were purchased from Aladdin Co. Ltd. The H_2O_2 assay kit, Z-VAD-FMK and GSH/GSSG kit were purchased from Beyotime Biotechnology Co. Ltd. The C11-BODIPY lipid peroxidation sensor was purchased from Life Science (InvitrogenTM, Pittsburg, USA). 2′,7′- DCFH-DA was purchased from Keygen Biotech Co. Ltd. (Nanjing, China). Necrostastin-1 and deferoxamine (DFO) mesylate were purchased from Target Molecule Corp. Ferrostatin-1 (Fer-1) was purchased from Aladdin Co. Ltd. Dimethyl sulfoxide (DMSO), 3-methyladenine (3-MA), thrombin and dihydroethidium (DHE) were purchased from Sigma. Foetal bovine serum (FBS) was purchased from Life Science (GibcoTM, Pittsburgh, USA). GPX4, NOX4 and *P*-gp antibodies were purchased from Abcam.

2.2. Synthesis of PAB@MIL-53 (PMNP) nanoparticles

280.2 mg FeCl$_3$·6H$_2$O and a certain amount (5/10/20 mg) of PAB were dissolved in ethanol for 10 min. Subsequently, add 172.5 mg H$_2$BDC dropwise into the solution within 10 min. Afterwards, stirred the mixture for 3 h and then centrifuged after 15 min. The obtained precipitate was washed with ethanol and water three times. Lastly, the brown products were washed with ethanol and centrifuged at 11,000 rpm (10 min).

2.3. In vitro cytotoxicity assay

MCF-7 and MCF-7/ADR cells were seeded onto a 96-well microplate at the density of 8×10^3 cells per well. After overnight culturing, both cells were treated with MNP, DOX, PAB, PMNP, PMNP-DOX@RBC nanoparticles for 24 h at various concentrations. Cell Counting Kit-8 (CCK-8) kit was added into each well for additional 1 h of incubation. After that, the absorbance at 450 nm was recorded by an Epoch2 microplate spectrophotometer (BioTek, USA) to calculate the cell viability. Experiments were performed in triplicate.

2.4. Assessment of ferroptosis

The cell cytotoxicity analysis was used to evaluate modality of PMNP-DOX@RBC-induced cell death [33]. Apoptosis, necroptosis and autophagy were identified via inhibitor Z-VAD-FMK (10 μM), necrostatin-1 (10 μM) and 3-MA (10 μM). Similarly, ferroptosis were studied via inhibitor ferrostatin-1 (Fer-1) (10 μM), or iron chelator deferoxamine (DFO) (100 μM). Briefly, MCF-7/ADR cells were seeded onto a 96-well microplate at the density of 8×10^3 cells per well. After overnight culturing, the cells were treated with PMNP-DOX@RBC nanoparticles (100 μg/mL) with various inhibitors for 24 h. CCK-8 kit was added into each well for additional 1 h of incubation. Afterwards, cell viability was calculated with the records of the absorbance at 450 nm.

2.5. Evaluation of the intracellular lipoperoxide accumulation

MCF-7 and MCF-7/ADR cells were seeded onto six-well plates. After overnight culturing, both were treated with various nanoparticles (MNP, PMNP, PMNP-DOX and PMNP-DOX@RBC) at the concentration of 100 μg/mL. For another 24 h incubation, wash the cells twice with PBS and
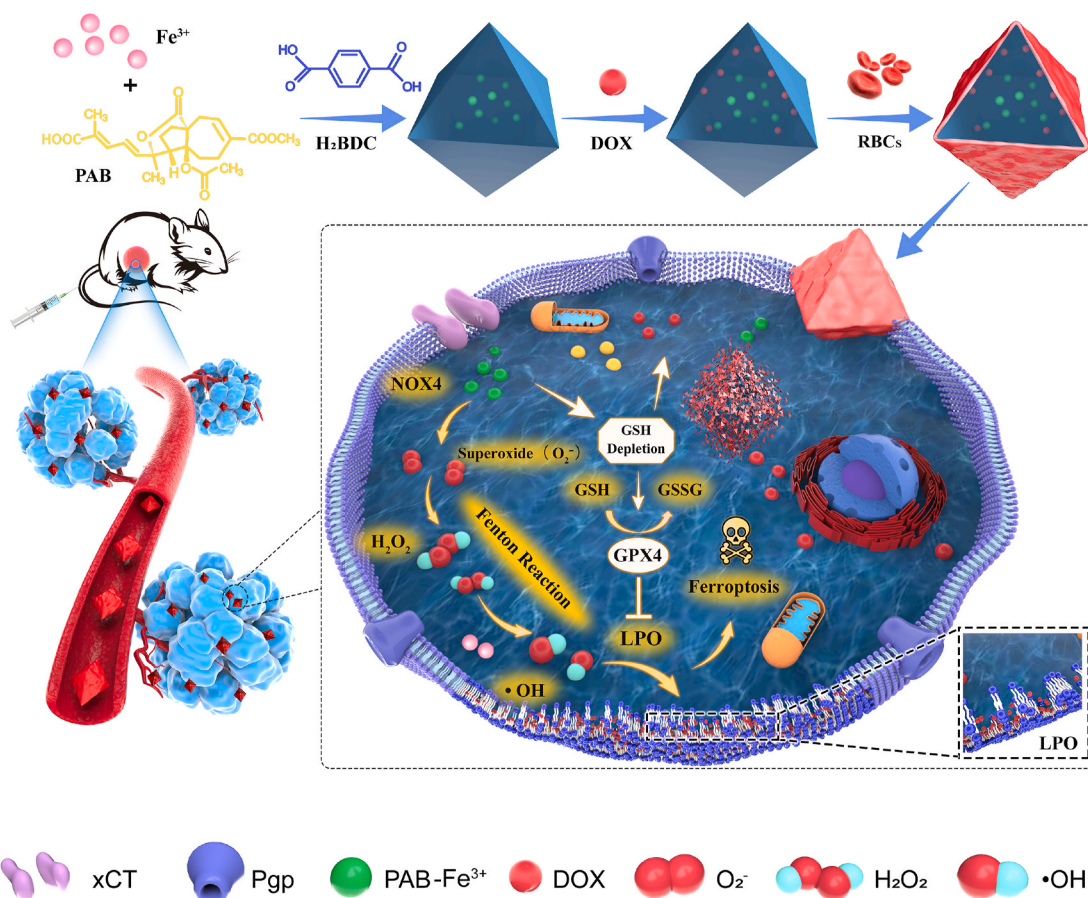
Fig. 1. Schematic illustration of the formation of MOF-membrane-camouflaged multi-drug-delivery nanoplatform for ferroptosis-based cancer therapy.

stained with the C11-BODIPY 581/591 probe (10 μM) at 37 °C for 20 min in a tissue culture incubator. Afterwards, resuspended the cells by 500 μL fresh PBS for three times, and analyzed cells with a flow cytometry.

2.6. Establishment of tumour models and tumour therapy

All animal experiments were performed in compliance with the "Guide for the Care and Use of Laboratory Animals" of the Institute of Laboratory Animal Resources and approved by the ethics committee of Fudan University. MCF-7/ADR cells were established by injecting 100 μL of PBS containing 1×10^7 cells into the subcutaneous tissue of the BALB/c female nude mice (4–6 weeks old). Various samples were then administered when the tumour size reached 80 mm^3. Briefly, MCF-7/ADR tumour-bearing mice were randomly divided into seven groups (each with five mice) and administrated by intravenous injection of PBS, MNP, PAB, DOX, PMNP, PMNP-DOX and PMNP-DOX@RBC with a 5 mg/kg equivalent DOX concentration. The injection was repeated by the injection schedule.

2.7. Safe evaluation

In the end of the efficacy study, all mice received euthanasia. Tumours and major organs were harvested and weighed for all groups. Beyond that, the harvested organs were made into H&E-stained tissue slices to monitor cytotoxicity. H&E-stained tissue sections were later observed under microscopes.

3. Results and discussion

3.1. Construction of defect structure of materials of institut Lavoisier-53 (MIL-53)

MIL-53(Fe) was synthesized according to the previously reported literature, with slight modification [34]. To regulate the size and morphology of MIL-53 (denoted as MNP), we varied the mass ratio of Fe^{3+} to H$_2$BDC from 0.5:1 to 4:1 (Table S1). When the ratio of Fe^{3+} to H$_2$BDC changed from 0.5:1 to 2:1, the average hydrodynamic diameter of MNP decrease from 215.1 to 891.5 nm, accompanied by a polydispersion index decrease from 0.442 to 0.126. As demonstrated by transmission electron microscopy (TEM) images (Fig. S1), the particles (MNP-III) are revealed the formation relatively uniform in size and shape at an Fe^{3+}:H$_2$BDC ratio of 2:1. The synthesis scheme of DSA-enabled MOF with encapsulated target drug is illustrated in Fig. 2a. Metal ions (Fe^{3+}) and guest drug molecules (carboxyl groups) self-assemble to form precursor complexes. Subsequently, organic linkers (H$_2$BDC) in *N,N*-dimethylformamide are added dropwise to form MOFs by the assembly of the metal ions and organic linkers. The structural defect contents of Fe-based MOFs were created by the reaction of Fe^{3+} and guest drug molecules. The guest drug molecules are confined during the formation of MOFs [35]. Using this DSA strategy, we investigated PAB [36] as a guest drug to develop a customizable and efficient nanoplatform, suggesting a general approach for the preparation of defect MOFs. We anticipated that the DSA-enabled MOF nanoplatform could be developed as a smart and highly stable system with substantially enhanced drug delivery.
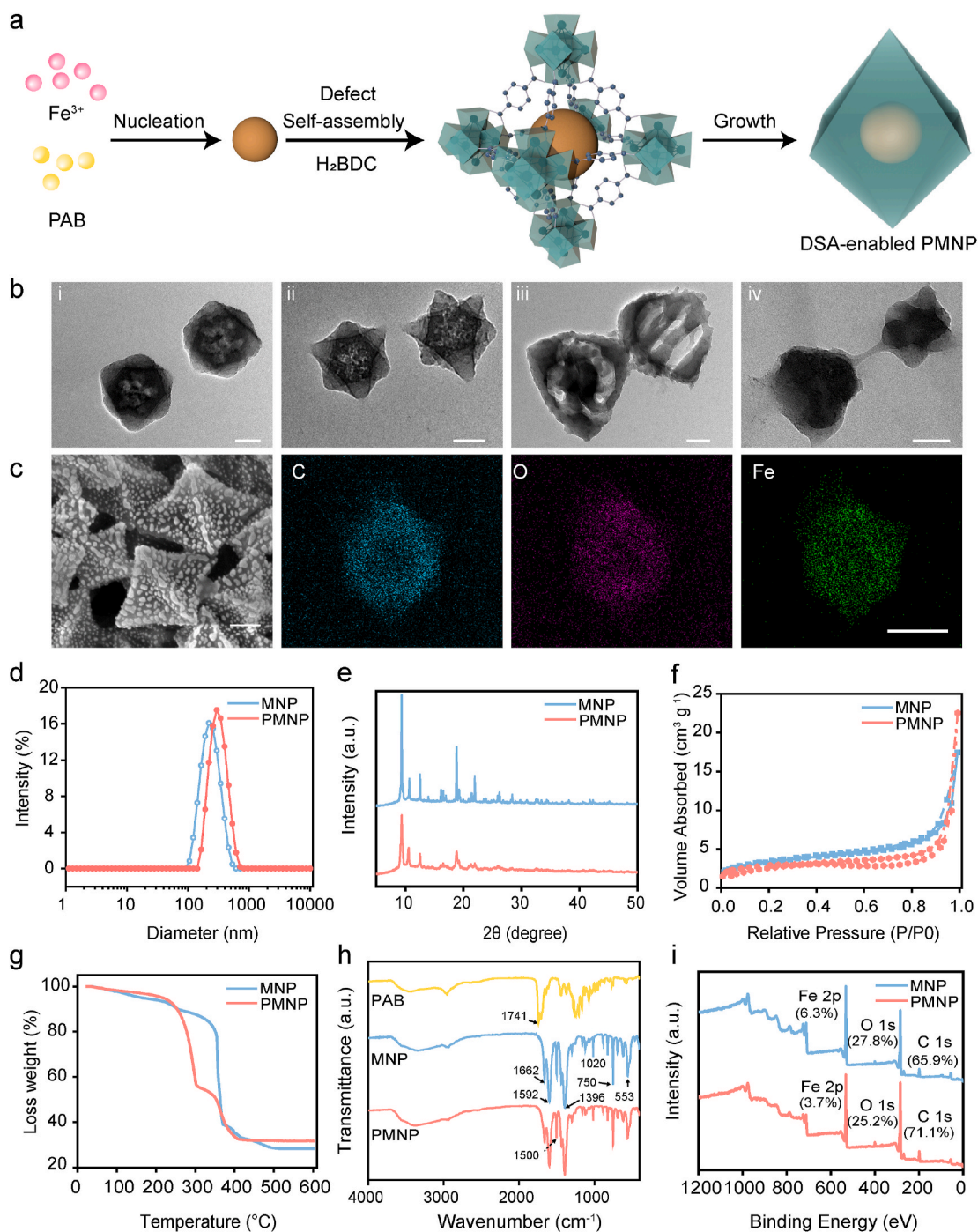
Fig. 2. Nanoparticle characterization. a, Schematic illustrations of the metal-organic framework (MOF) defect self-assembly (DSA) pathway. b, High-resolution TEM image of PMNP-5 (i), PMNP-10 (ii), PMNP-20 (iii) and PMNP-DOX@RBC (iv). Scale bar, 100 nm c, SEM image and elemental mapping images (C, O, and Fe) of PMNP-10. Scale bar, 100 nm d, Dynamic light scattering size of MNP and PMNP. e, Powder X-ray diffraction patterns of MNP and PMNP. f, The N_2 sorption isotherms of the MNP and PMNP. g, Thermogravimetric analysis. h, FTIR spectra of MNP and PMNP. i, XPS spectra of MNP and PMNP.

3.2. Construction and characterization of MOF-membrane-camouflaged nanoplatform

PMNP with different structural defect contents were prepared by the reaction of Fe^{3+} and PAB, with equivalents of PAB (5 mg, 10 mg, 20 mg) as the modulator, which was denoted as PMNP-5, PMNP-10 and PMNP-20 (Fig. 2b, Fig. S2 and Table S2). TEM images showed that each structure contained PAB that was fully MOF encapsulated, yet well dispersed, and revealed that the synthesized PMNP composite displays the same morphology as pure MIL-53 (Fig. S1). The scanning electron

microscopy (SEM) (Fig. 2c) images of PMNP clearly show uniform regular octahedral morphology. Dynamic light scattering (DLS) indicates that the particle size of PMNP with a slight change is hardly influenced by structural defects (Fig. 2d). In contrast to MNP, PMNP demonstrated structural defects with low contrast in the core of MOF crystals. Besides, the size of the in-situ defect structure was regulated by the pre-complex, which shows that using PAB as a modulator during the defect self-assembly pathway. As presented in Table S3 in the Supporting Information, the loading content of PAB can reach up to 22.9%. The particle size of PMNP in serum and RPMI-1640 cell medium increased slightly

within 24 h, and this demonstrates a good stability in different physiological mediums (Table S4). The powder X-ray diffraction (PXRD) pattern indicated that the MNP adopted an MIL-53 structure, while PMNP retained the same crystalline form as the pure MIL-53 (Fig. 2e) [37]. In contrast to pure MIL-53, the PMNP display slightly decreased, gravimetric Brunauer-Emmett-Teller (BET) surface areas, as expected, resulted from the contributions of PAB to the masses of the composites (Fig. 2f) [38].

To investigate whether the PAB is embedded within PMNP, thermogravimetric analysis (TGA) was carried out. TGA is one of the most straightforward methods that provide first-hand information to assess the existence of defects. Based on the TGA data (Fig. 2g), the defect has PAB in the composite. The first-stage decomposition of the PMNP composite in the air starts at 120 °C and finishes at approximately 310 °C, which is much lower than the decomposition temperature of the pure MIL-53 crystal (370 °C). Approximately 18% of weight loss occurs during the first stage, suggesting the decomposition of the PAB complex. As revealed by the Fourier transform infrared spectroscopy (FTIR) data in Fig. 2h, the characteristic absorption peaks of the MNP were observed at 1662, 1592, 1396, 1020, and 750 cm^{-1}, which could primarily come from the carboxylate group vibrations. This result follows the reported data reported in the literature [39]. In addition, PAB exhibits the characteristic infrared absorption peak of the stretching modes of carbonyls (1741 cm^{-1}). PMNP does not exhibit this peak, suggesting that PAB are embedded into MNP structural defects, consistent with the TEM and TGA results.

To further verify the components and structure, TEM elemental mapping images and X-ray photoelectron spectroscopy (XPS) results were evaluated. The TEM elemental mapping results showed a clear distribution of carbon, oxygen and iron elements, which confirmed the formation of Fe^{3+}-PAB precursor complexes via DSA. Furthermore, the XPS spectra (Fig. 2i) revealed that the Fe content in PMNP (3.7%) was much lower than that in MNP (6.3%), which was probably due to the structural defect contents. For the high resolution XPS spectrum of Fe 2p, the two peaks at binding energies of 711.5 and 725.4 eV were ascribed to Fe $2p_{3/2}$ and $2p_{1/2}$ respectively and were characteristic of ferric iron in MIL-53 (Fig. S3).

PMNP was coated with red blood cell (RBC) membranes via sonication and a physical extrusion strategy to encapsulate DOX in the pores of PMNP (PMNP-DOX@RBC), which prevented unexpected drug leakage during transport in the bloodstream [40]. Upon coating the PMNP with the RBC membrane, the core-shell morphology of PMNP@RBC was confirmed under TEM (Fig. 2b–iv). TEM visualization showed the presence of the membrane coatings over the PMNP. To prove this concept, we selected DOX as a model drug considering its remarkable chemotherapeutic effect on breast cancer. The loading content of DOX can reach up to 6.5%. The successful loading of DOX in MNP may result from the physical and hydrogen bonding interactions.

### 3.3. Evaluation of the efficacy of PMNP-DOX@RBC-induced cell death

Fig. S4 shows the drug release kinetics of DOX from PMNP-DOX@RBC. From the DOX release profiles, the release of DOX from PMNP-DOX@RBC is pH-responsive. When PMNP-DOX@RBC are dispersed in a pH 7.4 solution, only 27.9% of DOX is released within 24 h. As the pH of the solution decreases, the DOX release of PMNP-DOX@RBC nanoparticles increases. When the pH of the solution is 5.5, the DOX release amount of the nanoparticles can reach 70.3% in 24 h. Therefore, the MOF-membrane-camouflaged multi-drug-delivery nanoplatform can release drug under the acidic environment, but hardly release drug under the neutral environment, which is expected to achieve precise and efficient treatment of tumours.

We further evaluated the tumour-inhibiting effects of PMNP-DOX@RBC nanoparticles. The cytotoxic activity of MCF-7 cells was then quantitatively investigated using a CCK-8 assay. PMNP@RBC has also been added to the cell study in Fig. S5, which demonstrates that

PMNP@RBC group has the similar cytotoxicity with the PMNP group. As Fig. 3a shows, free DOX increased the cytotoxic activity in MCF-7 cells compared with that of the PAB group. After incubation with DOX at 5 µg/mL, the relative cell viability was dramatically reduced by approximately 64.9%, indicating a major role of cytotoxicity. To further elucidate the MDR reversal mechanism of PMNP-DOX@RBC, we assessed the cytotoxic effects of free DOX, PAB, PMNP-DOX and PMNP-DOX@RBC nanoparticles in MCF-7/ADR cells. As illustrated in Fig. 3b, MCF-7/ADR cells displayed higher resistance to DOX even at high concentrations. The half-maximum inhibitory concentration (IC_{50}) value of free DOX increased from ~500 ng/mL for sensitive MCF-7 cells to ~25,000 ng/mL for MCF-7/ADR cells [41]. By comparison, the viabilities of the MCF-7 and MCF-7/ADR cells decreased slightly by PAB at a relatively low concentration. Importantly, PMNP-DOX@RBC displays dose-dependent cytotoxicity to both MCF-7 and MCF-7/ADR cells, which suggests that PMNP-DOX@RBC exhibited the strongest ability to kill MDR breast cancer.

3.4. MOF-membrane-camouflaged nanoplatform amplifies oxidative stress

Generally, cytotoxic ROS, superoxide radicals ($O_2^{•-}$), hydroxyl radicals (•OH), hydrogen peroxide (H_2O_2), and singlet oxygen ($^1O_2$) play key roles in cell signalling and homeostasis. We supposed that PMNP-DOX@RBC could exhaust intracellular GSH and generate ROS concurrently, which would synergistically elevate intratumour oxidative stress. We thus investigated related-ROS activity in regulating oxidative stress. The effect of PMNP-DOX@RBC nanoparticles on oxidative stress-related factors in MCF-7/ADR cells was investigated. By comparison, PAB produced an approximately 2.2-fold increase in H_2O_2 (Fig. 3c), which contributed to upregulated expression of nicotinamide adenine dinucleotide phosphatase oxidase 4 (NOX4) enzymes. In the plasma membrane, NOX4 enzymes catalyze the production of $O_2^{•-}$ and H_2O_2 by transferring an electron from nicotinamide adenine dinucleotide phosphatase (NADPH) to molecular oxygen. However, iron-based nanoparticles, such as MNP, PMNP-DOX, and PMNP-DOX@RBC nanoparticles showed lower H_2O_2 levels. Iron-based MOFs are necessary for ROS-based cancer treatments. Through the Fenton reaction, highly toxic •OH can be generated in situ generated from catalyzing H_2O_2. Ferric ions could use H_2O_2 to generate •OH by the Fenton reaction. As described in the following equation,

$$Fe^{2+}+H_2O_2 \rightarrow Fe^{3+}+•OH + OH^-$$

$$Fe^{3+}+H_2O_2 \rightarrow Fe^{2+}+•OOH+H^+$$
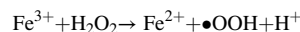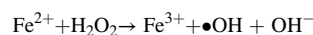
Notably, PMNP-DOX@RBC induced a vast amount of ROS as shown by the conspicuous green fluorescence in MCF-7/ADR cells. The intracellular ROS could be significantly improved (Fig. 3d) in the case of iron and H_2O_2 enrichment. To examine the production of •OH by the MOF-membrane-camouflaged nanoplatform at the cellular level, a 2',7'-dichlorofluoresc indiacetate (DCFH-DA) probe was employed as the fluorescent ROS indicator, as shown as in Fig. 3e. Both PMNP and PMNP-DOX@RBC groups showed enhanced ROS compared to the control, while the ROS could be greatly inhibited by the ferroptosis inhibitor ferrostatin-1 (Fer-1). The generation of Fe^{2+} ions was corroborated using a ferrorange probe, which could produce a bright fluorescent substance with Fe^{2+} ions. By comparison, the cells treated with MNP, PMNP, PMNP-DOX@RBC nanoparticles emitted enhanced fluorescence (Fig. 3f), suggesting a vast amount of Fe^{2+} ions generated via iron-based MOFs. Flow cytometry, as shown in Fig. 3g, revealed that the intensity of the red fluorescence detected by the dihydroethidium (DHE) superoxide probe was obviously elevated levels of $O_2^{•-}$ in the cells treated with PMNP-DOX@RBC for 6 h, whereas the $O_2^{•-}$ level in the cells treated with MNP remained unchanged. Activated NOX4 can catalyze the NADPH and oxygen into $NADP^+$ and $O_2^{•-}$. Then the $O_2^{•-}$ undergoes disproportionation reactions to generate H_2O_2 and O_2 catalyzed by PAB.
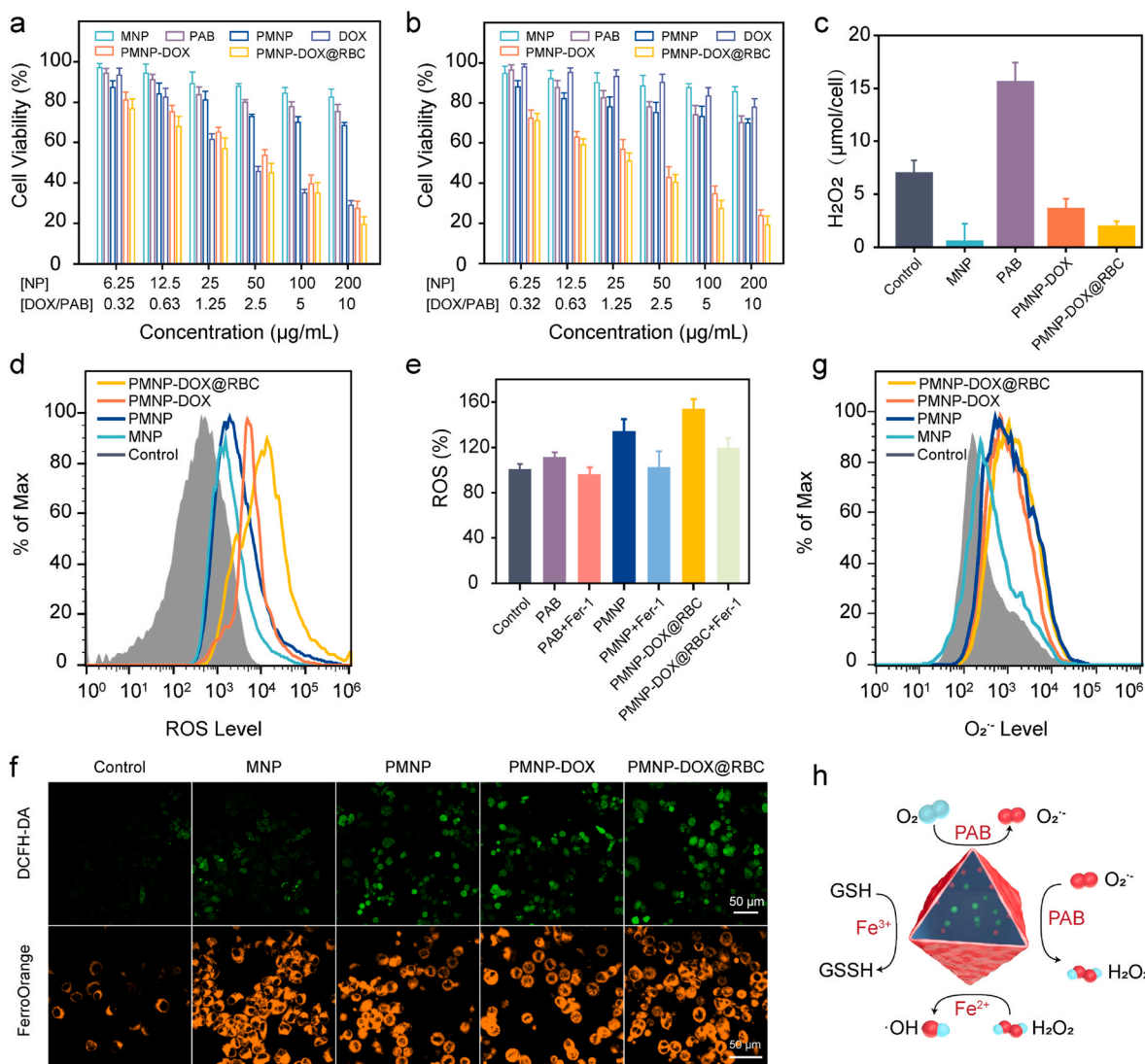
Fig. 3. *In vitro* cytotoxicity and mechanism of ferroptosis induced by MOF-membrane-camouflaged nanoplatform. Cell viability of MCF-7 (a) and MCF-7/ADR cells (b) treated with different concentrations of free DOX, PAB, MNP, PMNP, PMNP-DOX and PMNP-DOX@RBC, respectively. c, Intracellular H_2O_2 levels in MCF-7/ADR cells treated with different formulations (MNP, PAB, PMNP-DOX and PMNP-DOX@RBC) by hydrogen peroxide assay kit; n = 3. ROS (d) and superoxide (g) production evaluated by flow cytometry using DCFH-DA and dihydroethidium probes. e, reactive oxygen species assay kit analysis of MCF-7/ADR cells after treatment with formulations nanoparticles. f, Representative confocal fluorescence microscopy images of ROS and Fe^{2+}. Staining assay of MCF-7/ADR cells via DCFH-DA and FerroOrange staining. h, Schematic illustration of the activity of PMNP-DOX@RBC.

As Fig. 3h reveals the ROS generation by cascade reactions.

### 3.5. MOF-membrane-camouflaged nanoplatform depletes GSH

For furthering understanding of the importance of GSH in repair oxidative damage, we then investigated the GSH level and GPX4 changes. Western blot analysis confirmed that GPX4 protein expression was the lowest in the cells treated with PMNP-DOX@RBC nanoparticles. In particular, ferric ions (Fe^{3+}) can deplete GSH through catalyzed reductive reactions to produce ferrous ions (Fe^{2+}) and oxidized glutathione (GSSG). ($2Fe^{3+}+2GSH \rightarrow 2Fe^{2+}+GSSG+2H^+$) [42], especially at high levels of GSH in tumour cells [43]. The GSH depletion property of the self-assembly-enabled MOF-membrane-camouflaged multi-drug-delivery nanoplatform was evaluated by measuring the intracellular GSH levels using a GSH/GSSG kit. The intracellular GSH (Fig. 4a) was decreased by PMNP-DOX@RBC [44]. Tumour cells are recognized to be abundant with GSH to protect them from ROS damage [45]. PAB can deplete GSH contributed to PAB-induced accumulation of H_2O_2 and lipid peroxide [18]. As Fig. 4a shown, PMNP, PMNP-DOX and PMNP-DOX@RBC has relatively

low GSH compared to the control group. Accordingly, PMNP, PMNP-DOX, and PMNP-DOX@RBC could improve the level of ROS. In particular, DOX could induce more ROS, accompanying higher lipid peroxide levels.

To summarize, all these results demonstrate the imitating activities of the DSA-enabled nanoplatform, which catalyzes GSH depletion and ROS generation, respectively, by cascade reactions, as shown in Fig. 3h. As a result, PMNP-DOX@RBC could realize GSH depletion and the generation of ROS, which is promising for in vivo cancer therapy.

3.6. Mechanism underlying MOF-membrane-camouflaged nanoplatform-induced cell death

To explore the cell death mechanism by the MOF-membrane-camouflaged nanoplatform, we further analyzed possible death modes, such as apoptosis, ferroptosis, autophagy, and necroptosis, in MCF-7/ADR cells. The apoptosis inhibitor carbobenzoxy-valyl-alanyl-aspartyl-[O-methyl]-fluoromethylketone (Z-VAD-FMK), autophagy inhibitor 3-methladenine (3-MA) and necroptosis inhibitor necrostatin-1 did not improve the viability of PMNP-DOX@RBC-treated MCF-7/ADR cells
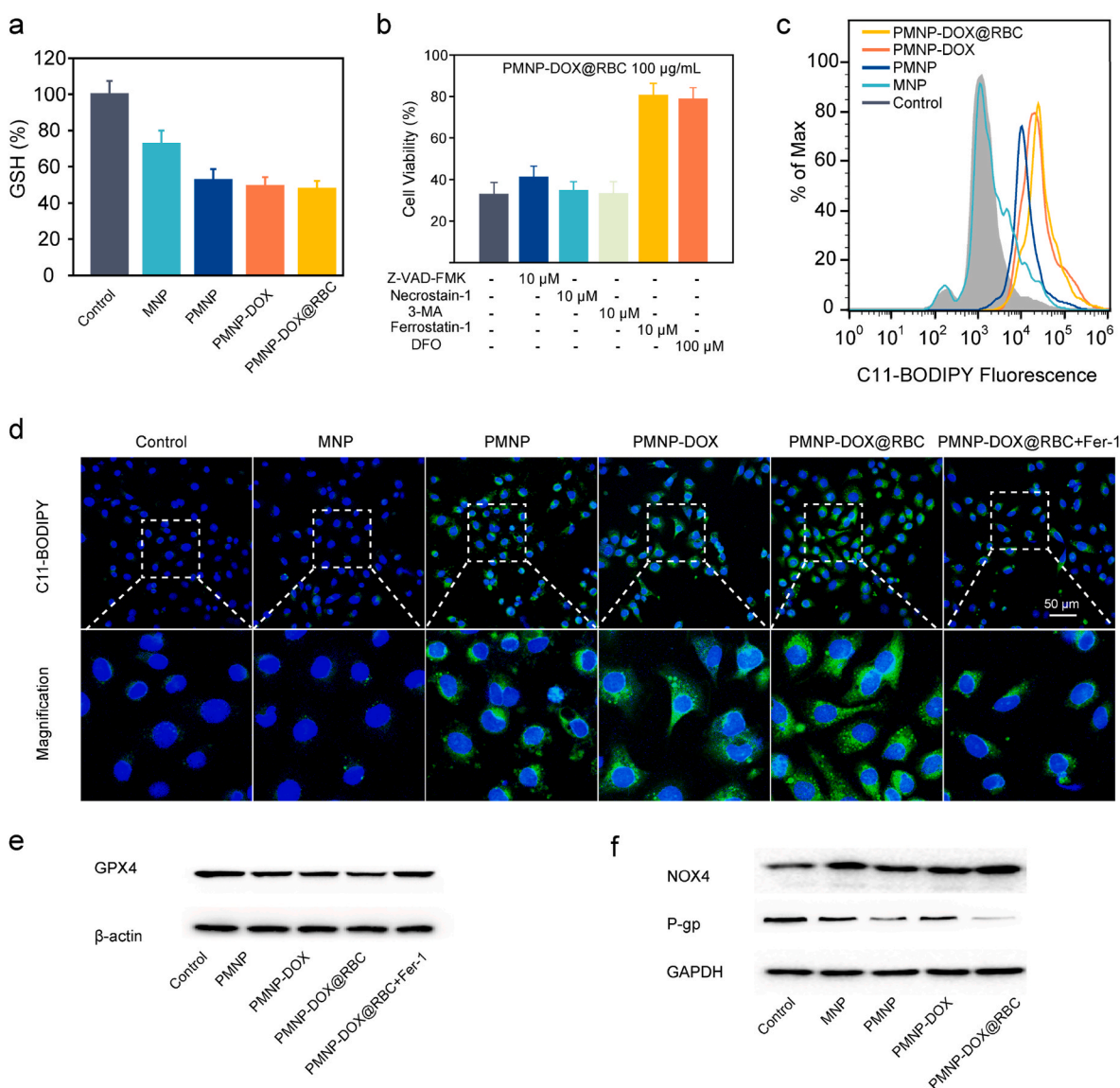
Fig. 4. a, Intracellular GSH levels in MCF-7/ADR cells treated with different formulations (MNP, PMNP, PMNP-DOX and PMNP-DOX@RBC); n = 3. b, Cell viability in the presence of apoptosis inhibitor, necroptosis-specific inhibitor, and autophagy inhibitor, ferroptosis inhibitor, respectively. c, Flow cytometry analysis of MCF-7/ADR cells lipid ROS production evaluated using C11-BODIPY probes. d, Representative confocal fluorescence microscopy images of LPO. Staining assay of MCF-7/ADR cells via C11-BODIPY staining. Western blot analysis of the expression of key ferroptosis makers, including GPX4 (e), NOX4(f), and *P*-gp (f) in MCF-7/ADR cells treated with different formulations.

(Fig. 4b), indicating that PMNP-DOX@RBC did not induce necroptosis or autophagy in MCF-7/ADR cells. Notably, both Fer-1 and the iron chelator deferoxamine (DFO) significantly upregulated the viability of MCF-7/ADR cells, indicating that the main pathway of ferroptosis occurred in PMNP-DOX@RBC-treated cells.

3.7. Evaluation of the efficacy of MOF-membrane-camouflaged-induced ferroptosis

Given the potent GSH and ROS in ferroptotic activity, we first evaluated the GSH activity of PMNP-DOX@RBC because GSH plays an important role in the ROS generation/depletion process.

Hence, we tested the lipid peroxidation of •OH induction in MCF-7/ADR cells, as assayed by flow cytometry using a C11-BODIPY probe. We noticed that PMNP-DOX@RBC significantly upregulated the lipid peroxidation level in MCF-7/ADR cells. Furthermore, the strongest C11-BODIPY fluorescence was detected at the plasma membranes (Fig. 4c and d), elucidating the occurrence of lipid peroxidation. We found that

PMNP-DOX@RBC significantly elevated the lipid peroxidation level in MCF-7/ADR cells. These observations are agreement with the lipoperoxide measurement and CCK-8 assay results and confirm the activation of ferroptosis pathways.

To further assess the molecular mechanism of MCF-7 cells, confocal laser scanning microscopy studies were constructed, as shown in Fig. S6. Cellular effects of ferroptosis were investigated using a C11-BODIPY probe, suggesting a similar result as MCF-7/ADR cells. In comparison, for MCF-7/ADR cells incubated with PMNP-DOX@RBC nanoparticles, strong fluorescence could be found, which suggests that PMNP-DOX@RBC nanoparticles were more sensitive to drug-resistant cells.

Since GSH could be used by GPX4 to repair oxidative damage, we further investigated GSH and GPX4 (Fig. 4e) treated by PMNP-DOX@RBC. Compared with the control group, GSH levels of PMNP-DOX@RBC treatment significantly decreased, which all contributed to PMNP-DOX@RBC treatment. Western blot analysis confirmed that GPX4 protein expression was the lowest in the cells treated with PMNP-DOX@RBC group.

To further validate the ferroptosis mechanism, we applied Western blot analysis. Notably, the cells treated with PMNP-DOX@RBC highly expressed NOX4 protein compared with the other control groups (Fig. 4f). We further used bio-TEM to assess the cell and subcellular morphology induced by ferroptosis. TEM images showed that PMNP-DOX@RBCs were located in the endosomes/lysosomes and cytoplasm and finally degraded in the cytoplasm (Fig. 5a). Apparent shrinkage of the mitochondrial dimensions and chromatin condensation could be clearly observed from the magnified figure, illustrating the combination of cell ferroptosis and apoptosis.

It has been reported that cell ferroptosis is associated with an increased membrane density of mitochondria. To investigate whether the mitochondria were damaged after PMNP-DOX@RBC treatment, MitoTracker Red CMXRos staining was carried out to monitor mitochondrial membrane potential changes (Fig. 5b). It is well established that PMNP-DOX@RBC showed an increased MitoTracker Red CMXRos signal, which indicated that the cristae of mitochondria almost disappeared. These results prove that PMNP-DOX@RBC treatment disrupted mitochondrial morphology.

3.8. Molecular mechanism underlying the ferroptosis-mediated MDR reversal effect in vitro

Benefiting from the MOF-membrane-camouflaged nanoplatform, DOX can be loaded into the pores directly. To elucidate the in vitro mechanism of PMNP-DOX@RBC underlying the reversal of

chemotherapy resistance, the cytotoxic activity of the composite was determined. Significant growth inhibition of MCF-7 cells was discerned when the cells were incubated with either free DOX or PMNP-DOX@RBC nanoparticles at a higher DOX concentration, and PMNP-DOX@RBC nanoparticles were significantly more cytotoxic to MCF-7/ADR cells than free DOX at an equivalent DOX dosage, which proves that PMNP-DOX@RBC display enough ability to eliminate cancer cells and overcome MDR. Free DOX moves into MCF-7/ADR cells through a flip-flop mechanism and is extruded by the overexpressing efflux *P*-gp [46]. As shown in Fig. 4f, western blotting results of *P*-gp expression in MCF-7/ADR cells after treatment with PMNP-DOX@RBC showed dramatic downregulation. Both the PMNP and PMNP-DOX@RBC groups exhibited lower *P*-gp expression levels contributed from PAB. Together, these results show that PMNP-DOX@RBC elevates intracellular oxidative stress and depletes GSH to induce ferroptosis, which could downregulate *P*-gp by regulating the fluidity and permeability of the cell membrane and then reduce drug resistance. The regulation mechanism of ferroptosis is still not fully clear, but preliminary research has already identified in the metabolic processes involved as shown in Fig. 5c.

3.9. In vivo evaluation of the antitumour efficacy of the complementary ferroptosis chemotherapy

As shown in the pharmacokinetics results (Fig. S7), in the first 4 h, there was an 18% ID/g drop in the blood iron concentration in the blood. There is a slow decrease in the following 24 h, which indicates the
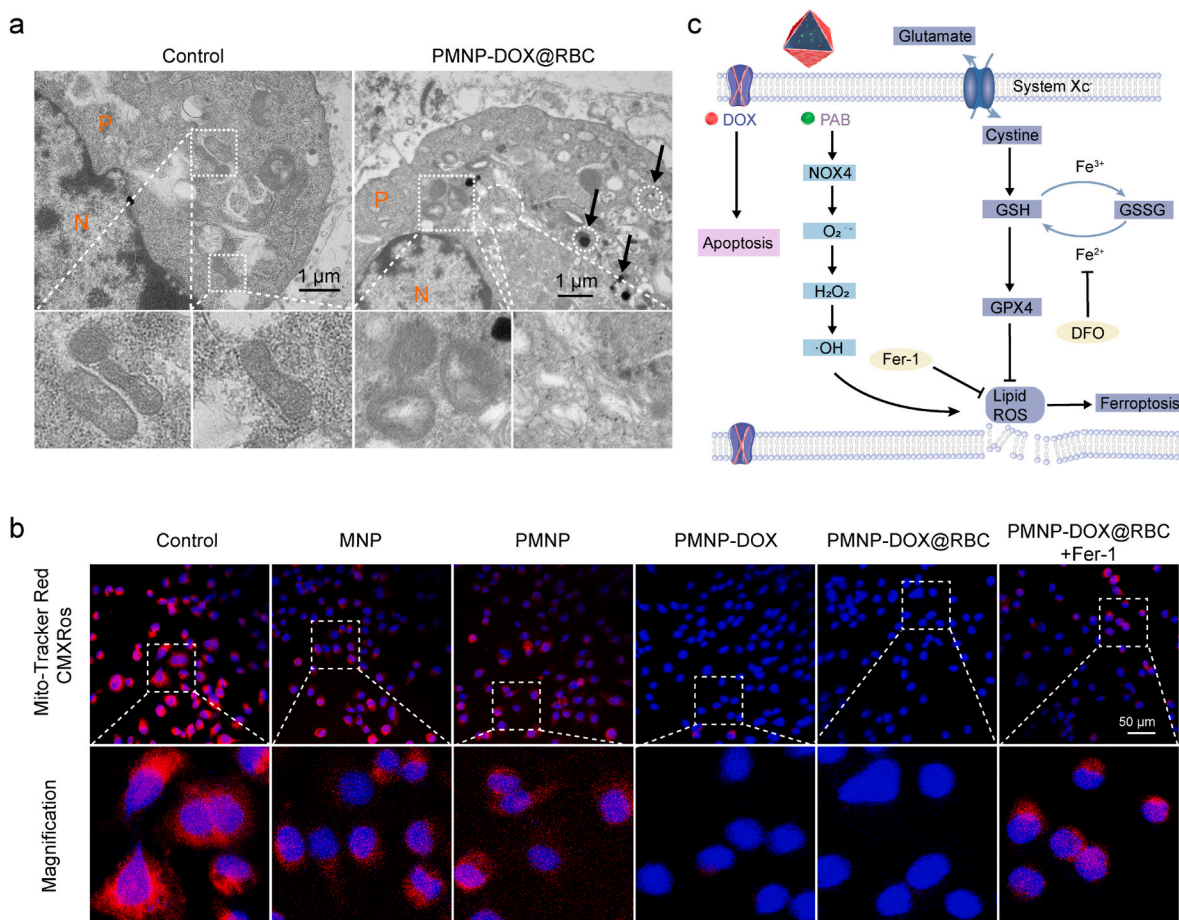
Fig. 5. a, Bio-TEM images of the MCF-7/ADR cells co-incubated with PMNP-DOX@RBC nanoparticles. The circle and box dashed region indicate the PMNP-DOX@RBC located inside the cells and magnified views of mitochondria. The cell plasma and nucleus are denoted as P and N, respectively. b, The mitochondrial potential changes imaged by Mito-Tracker Red CMXRos staining. MCF-7/ADR cells were treated with PBS as control, MNP, PMNP, PMNP-DOX, PMNP-DOX@RBC, and PMNP-DOX@RBC + Fer-1. c, The proposed molecular mechanism underlying MOF-membrane-camouflaged multi-drug-delivery nanoplatform-induced synergistic ferroptosis/apoptosis cell death.

slowed distribution of nanoparticles and the tumour accumulation. Besides, biodistribution data (Fig. S8) shows that there is an increase in kidney and spleen iron concentration, which may have undergone metabolism and cleared out through kidney and spleen in 24 h.

Furthermore, the accumulation of PMNP-DOX@RBC in visceral organs and tumours was investigated by Fe content measurement. It was observed that there was $6.4 \pm 0.3\%$ ID g^{-1} of PMNP-DOX@RBC in the tumours after 4 h of injection, and then decreased to $5.6 \pm 0.8\%$ ID g^{-1}
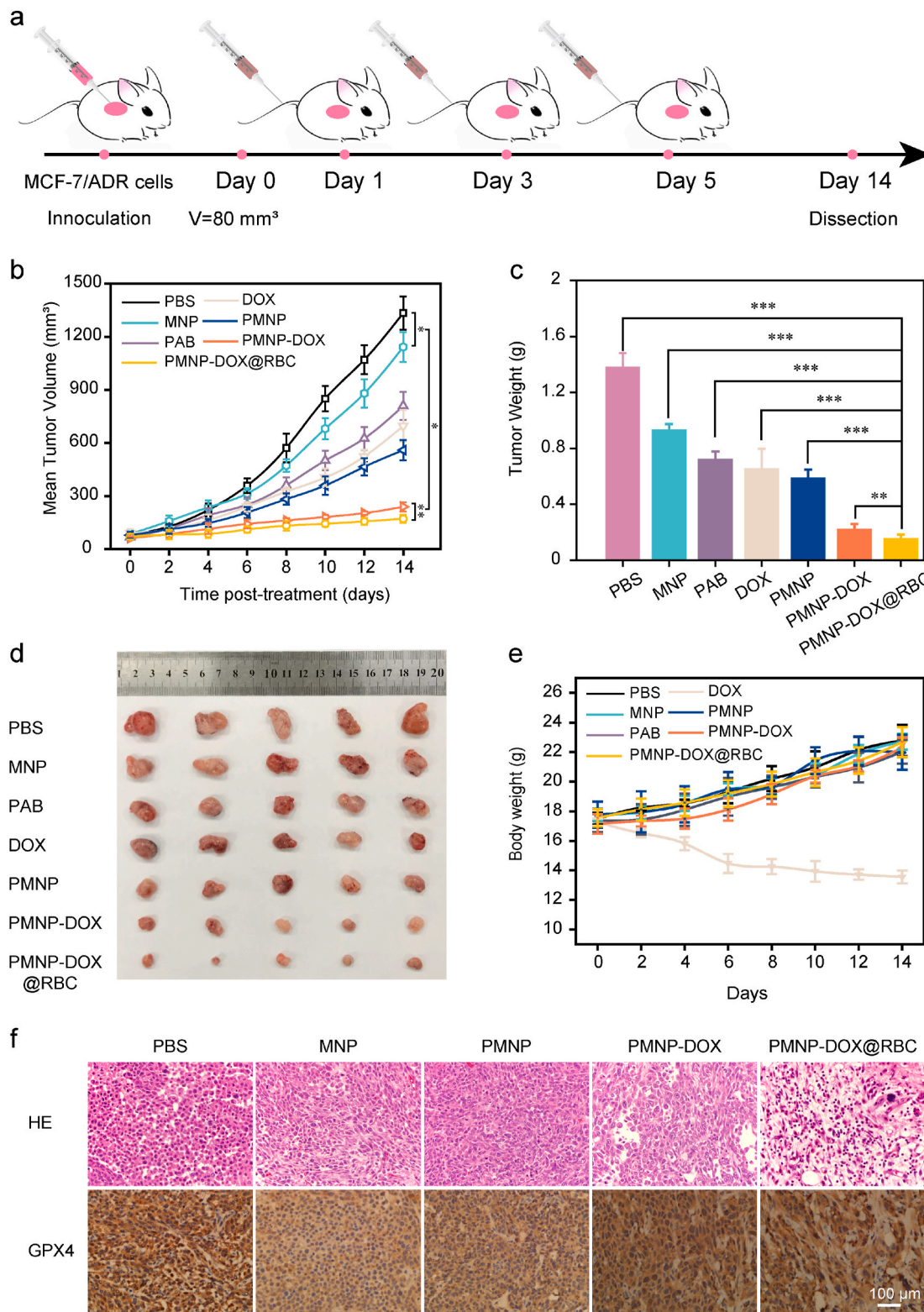
Fig. 6. Anticancer efficacy of MOF-membrane-camouflaged nanoplatform against MCF-7/ADR tumours. PBS, MNP, free DOX, free PAB, PMNP, PMNP-DOX, and PMNP-DOX@RBC nanoparticles were intravenous injected on days 1, 3, and 5. a, Injection schedule. Tumour volume progression (b) and body weight change (e) within the 14-day observation period (n = 5). Images of tumour weight (c) and excised tumours (d) on day 14 (n = 5). *P < 0.05, **P < 0.01, ***P < 0.001. H&E-stained and GPX4-stained (f) tumour tissues harvested on the 14th day.

after 24 h, indicating the good tumour-targeting ability.

Encouraged by the potency of PMNP-DOX@RBC nanoparticles in vitro, we further assessed their efficacy in inhibiting tumour growth in vivo. Nude mice with MCF-7/ADR xenografts were separated into seven groups (five mice each, ~20 g) and treated with PBS, MNP, free DOX, free PAB, PMNP PMNP-DOX and PMNP-DOX@RBC nanoparticles, and equivalent amounts of DOX or carrier substrates were ensured in each group. Fig. 6a presents a schematic depiction of the injection schedule. The in vivo antitumour efficacy was first estimated by Fig. 6b, and the PMNP-DOX@RBC group presented the highest tumour inhibition capacity among the seven groups. Specifically, the average volume of MCF-7/ADR tumours treated by PMNP-DOX@RBC for 14 days was only 171.6 mm^3, with an average weight of 0.13 g, which is much lower than those of the free DOX group (696.4 mm^3 and 0.69 g, respectively) (Fig. 6b and c). As shown in Fig. 6d, there was no significant antitumour efficacy in the PBS groups, while the tumour inhibition rate of the DOX group was 47%, which was probably because of constant weight loss. However, in the PMNP-DOX group, the antitumour rate calculated from tumour weight was ~82%. When coated with the RBC membrane, the antitumour rate of the PMNP-DOX@RBC group was improved to almost 87%, indicating that PMNP-DOX@RBC is a promising therapeutic agent in oncotherapy.

We further evaluated the potential side effects of repetitive injections. The changes in mouse weight were recorded every other day. By comparison, the DOX group had apparent weight loss after approximately 4 days, which was only 13.5 g at 14th day. The weight loss also confirms that free DOX has severe toxicity to heart muscle. However, the body weight of Fig. 6e for the PMNP-DOX@RBC and PMNP-DOX groups remained at 22.7 and 22.3 g, respectively, which was equal to the control group (22.8 g). Compared to the weight loss of the DOX group, the minor weight loss in the PMNP-DOX@RBC groups suggests that biomimetic nanostructure could markedly ameliorate cytotoxicity induced by DOX. The histological examination data demonstrate that PMNP-DOX@RBC nanoparticles have good biocompatibility, which may help to greatly expand the utility of MOF-membrane-camouflaged nanoplatform, facilitating potential clinical applications.

Furthermore, histological examination using haematoxylin and eosin (H&E) demonstrated that the MOF-membrane-camouflaged nanoplatform did not cause any observable abnormalities (Fig. 6f). In addition, GPX4 staining revealed the molecular mechanism of ferroptosis. These findings above consistently suggest that MOF-membrane-camouflaged nanoplatforms are of great importance to enhance the combined efficacy of ferroptosis and apoptosis to overcome resistance.

4. Conclusion

In conclusion, we report the application of the defect self-assembly-enabled MOF-membrane-camouflaged nanoplatform to address multidrug delivery. This approach provides simultaneous delivery of iron sources, ferroptosis inducers, drugs and enhanced circulation carriers to address MDR in malignant tumours. The embedded PAB-Fe^{3+} complexation within defect nanostructures could protect the guest molecules from oxidative stress in a physiological environment and prevent unexpected drug leakage during transport in bloodstream. The RBC membrane coating could prolong the blood retention time and immune escape capabilities. The resultant MOF-membrane-camouflaged nanoplatform could be degraded by the tumour microenvironment and act in synergy with the simultaneously released Fe^{3+} and PAB to amplify ferroptosis damage. Ferroptosis is driven by oxidative phospholipid damage, which could regulate the fluidity and permeability of the cell membrane to downregulate *P*-gp protein expression and then reduce drug resistance. However, the MOF-membrane-camouflaged nanoplatform could consume GSH, amplify ROS oxidative stress, and carry out tumour cell death by means of a complementary ferroptosis/apoptosis mechanism. Moving forward, dual ferroptosis/apoptosis treatment to tackle resistance should promise the

development of effective tumour therapies. The new concept of defect self-assembly-enabled MOF-membrane-camouflaged nanoplatform creates a new path to build multifunctional delivery systems for various applications.

CRediT authorship contribution statement

Haibao Peng: Conceptualization, Methodology, Investigation, Formal analysis, Data curation, Writing – original draft, Writing – review & editing, Funding acquisition. **Xingcai Zhang:** Investigation, Formal analysis, Writing – review & editing. **Peng Yang:** Methodology, Formal analysis, Investigation, Resources, Data curation. **Jiaxu Zhao:** Methodology, Formal analysis. **Wei Zhang:** Investigation, Resources, Data curation. **Nianping Feng:** Supervision, Methodology, Resources. **Wuli Yang:** Project administration, Project design, Funding acquisition, Writing – review & editing. **Jing Tang:** Writing – review & editing, Supervision, Project administration.

Declaration of competing interest

We declare that we have no financial and personal relationships with other people or organizations that can inappropriately influence our work, there is no professional or other personal interest of any nature or kind in any product, service and/or company that could be construed as influencing the position presented in, or the review of, the manuscript entitled.

Acknowledgements

Appendix A. Supplementary data

Supplementary data to this article can be found online at https://doi.org/10.1016/j.bioactmat.2021.12.018.

References

[1] R.L. Siegel, K.D. Miller, A. Jemal, Cancer statistics, 2020, Ca - Cancer J. Clin. 70 (2020) 7–30.
[2] N. Gong, X. Ma, Y. Ye, Q. Zhou, X. Chen, X. Tan, S. Yao, S. Huo, T. Zhang, S. Chen, X. Teng, X. Hu, J. Yu, Y. Gan, H. Jiang, J. Li, X.J. Liang, Carbon-dot-supported atomically dispersed gold as a mitochondrial oxidative stress amplifier for cancer treatment, Nat. Nanotechnol. 14 (2019) 379–387.
[3] X. Han, S.F. Shen, Q. Fan, G.J. Chen, E. Archibong, G. Dotti, Z. Liu, Z. Gu, C. Wang, Red blood cell-derived nanoerythrosome for antigen delivery with enhanced cancer immunotherapy, Sci. Adv. 5 (2019), eaaw6870.
[4] R. Pisa, T.M. Kapoor, Chemical strategies to overcome resistance against targeted anticancer therapeutics, Nat. Chem. Biol. 16 (2020) 817–825.
[5] J.R. Riordan, K. Deuchars, N. Kartner, N. Alon, J. Trent, V. Ling, Amplification of P-glycoprotein genes in multidrug-resistant mammalian-cell lines, Nature 316 (1985) 817–819.
[6] G. Szakacs, J.K. Paterson, J.A. Ludwig, C. Booth-Genthe, M.M. Gottesman, Targeting multidrug resistance in cancer, Nat. Rev. Drug Discov. 5 (2006) 219–234.
[7] D.S. Wei, Y.J. Yu, X.C. Zhang, Y.H. Wang, H. Chen, Y. Zhao, F.Y. Wang, G.H. Rong, W.W. Wang, X. Kang, J. Cai, Z.H. Wang, J.Y. Yin, M. Hanif, Y.B. Sun, G.F. Zha, L. X. Li, G.H. Nie, H.H. Xiao, Breaking the intracellular redox balance with diselenium nanoparticles for maximizing chemotherapy efficacy on patient-derived xenograft models, ACS Nano 14 (2020) 16984–16996.
[8] C. Gorrini, I.S. Harris, T.W. Mak, Modulation of oxidative stress as an anticancer strategy, Nat. Rev. Drug Discov. 12 (2013) 931–947.
[9] S. Kwon, H. Ko, D.G. You, K. Kataoka, J.H. Park, Nanomedicines for reactive oxygen species mediated approach: an emerging paradigm for cancer treatment, Acc. Chem. Res. 52 (2019) 1771–1782.

[10] S.J. Dixon, K.M. Lemberg, M.R. Lamprecht, R. Skouta, E.M. Zaitsev, C.E. Gleason, D.N. Patel, A.J. Bauer, A.M. Cantley, W.S. Yang, B. Morrison 3rd, B.R. Stockwell, Ferroptosis: an iron-dependent form of nonapoptotic cell death, Cell 149 (2012) 1060–1072.

[11] B.R. Stockwell, J.P.F. Angeli, H. Bayir, A.I. Bush, M. Conrad, S.J. Dixon, S. Fulda, S. Gascon, S.K. Hatzios, V.E. Kagan, K. Noel, X.J. Jiang, A. Linkermann, M. E. Murphy, M. Overholtzer, A. Oyagi, G.C. Pagnussat, J. Park, Q. Ran, C. S. Rosenfeld, K. Salnikow, D.L. Tang, F.M. Torti, S.V. Torti, S. Toyokuni, K. A. Woerpel, D.D. Zhang, Ferroptosis: a regulated cell death nexus linking metabolism, redox biology and disease, Cell 171 (2017) 273–285.

[12] X.X. Yao, R.H. Xie, Y.B. Cao, J. Tang, Y.Z. Men, H.B. Peng, W.L. Yang, Simvastatin induced ferroptosis for triple-negative breast cancer therapy, J. Nanobiotechnol. 19 (2021) 14.

[13] X. Jiang, B.R. Stockwell, M. Conrad, Ferroptosis: mechanisms, biology and role in disease, Nat. Rev. Mol. Cell Biol. 22 (2021) 266–282.

[14] J.P. Friedmann Angeli, M. Schneider, B. Proneth, Y.Y. Tyurina, V.A. Tyurin, V. J. Hammond, N. Herbach, M. Aichler, A. Walch, E. Eggenhofer, D. Basavarajappa, O. Radmark, S. Kobayashi, T. Seibt, H. Beck, F. Neff, I. Esposito, R. Wanke, H. Forster, O. Yefremova, M. Heinrichmeyer, G.W. Bornkamm, E.K. Geissler, S. B. Thomas, B.R. Stockwell, V.B. O'Donnell, V.E. Kagan, J.A. Schick, M. Conrad, Inactivation of the ferroptosis regulator GPX4 triggers acute renal failure in mice, Nat. Cell Biol. 16 (2014) 1180–1191.

[15] L. Su, R.C. Li, S. Khan, R. Clanton, F.W. Zhang, Y.N. Lin, Y. Song, H. Wang, J. W. Fan, S. Hernandez, A.S. Butters, G. Akabani, R. MacLoughlin, J. Smolen, K. L. Wooley, Chemical design of both a glutathione-sensitive dimeric drug guest and a glucose-derived nanocarrier host to achieve enhanced osteosarcoma lung metastatic anticancer selectivity, J. Am. Chem. Soc. 140 (2018) 1438–1446.

[16] X. Wan, L. Song, W. Pan, H. Zhong, N. Li, B. Tang, Tumor-targeted cascade nanoreactor based on metal-organic frameworks for synergistic ferroptosis-starvation anticancer therapy, ACS Nano 14 (2020) 11017–11028.

[17] P. Chiu, L.T. Leung, B.C. Ko, Pseudolaric acids: isolation, bioactivity and synthetic studies, Nat. Prod. Rep. 27 (2010) 1066–1083.

[18] C. Wen, J. Chen, D. Zhang, H. Wang, J. Che, Q. Qin, L. He, Z. Cai, M. Lin, Q. Lou, L. Huang, D. Chen, A. Iwamoto, D. Ren, L. Wang, P. Lan, J. Wang, H. Liu, X. Yang, Pseudolaric acid B induces mitotic arrest and apoptosis in both 5-fluorouracil-sensitive and -resistant colorectal cancer cells, Cancer Lett. 383 (2016) 295–308.

[19] D. Wang, Y. Xin, Y. Tian, W. Li, D. Sun, Y. Yang, Pseudolaric acid B inhibits gastric cancer cell metastasis in vitro and in haematogenous dissemination model through PI3K/AKT, ERK1/2 and mitochondria-mediated apoptosis pathways, Exp. Cell Res. 352 (2017) 34–44.

[20] Z. Wang, Y. Ding, X. Wang, S. Lu, C. Wang, C. He, L. Wang, M. Piao, G. Chi, Y. Luo, P. Ge, Pseudolaric acid B triggers ferroptosis in glioma cells via activation of Nox4 and inhibition of xCT, Cancer Lett. 428 (2018) 21–33.

[21] J.P. Friedmann Angeli, D.V. Krysko, M. Conrad, Ferroptosis at the crossroads of cancer-acquired drug resistance and immune evasion, Nat. Rev. Cancer 19 (2019) 405–414.

[22] H. Furukawa, K.E. Cordova, M. O'Keeffe, O.M. Yaghi, The chemistry and applications of metal-organic frameworks, Science 341 (2013) 1230444.

[23] L. Jiao, J.Y.R. Seow, W.S. Skinner, Z.U. Wang, H.L. Jiang, Metal-organic frameworks: structures and functional applications, Mater. Today 27 (2019) 43–68.

[24] J. Fu, L. Liang, L. Qiu, In situ generated gold nanoparticle hybrid polymersomes for water-soluble chemotherapeutics: inhibited leakage and pH-responsive intracellular release, Adv. Funct. Mater. 27 (2017) 1604981.

[25] Y. Fu, Z. Kang, W. Cao, J. Yin, Y. Tu, J. Li, H. Guan, Y. Wang, Q. Wang, X. Kong, Defect-assisted loading and docking conformations of pharmaceuticals in metal-organic frameworks, Angew. Chem. Int. Ed. 60 (2021) 7719–7727.

[26] S. Dissegna, K. Epp, W.R. Heinz, G. Kieslich, R.A. Fischer, Defective metal-organic frameworks, Adv. Mater. 30 (2018), e1704501.

[27] I.A. Lazaro, C.J.R. Wells, R.S. Forgan, Multivariate modulation of the Zr MOF UiO-66 for defect-controlled combination anticancer drug delivery, Angew. Chem. Int. Ed. 59 (2020) 5211–5217.

[28] B. Yang, L. Ding, H. Yao, Y. Chen, J. Shi, A metal-organic framework (MOF) fenton nanoagent-enabled nanocatalytic cancer therapy in synergy with autophagy inhibition, Adv. Mater. (2020), e1907152.

[29] J.S. Meng, J.T. Li, J.S. Liu, X.C. Zhang, G.P. Jiang, L. Ma, Z.Y. Hu, S.B. Xi, Y. L. Zhao, M.Y. Yan, P.Y. Wang, X. Liu, Q.D. Li, J.Z. Liu, T.P. Wu, L.Q. Mai, Universal approach to fabricating graphene-supported single-atom catalysts from doped ZnO solid solutions, ACS Cent. Sci. 6 (2020) 1431–1440.

[30] J. Yang, X. Zhang, C. Liu, Z. Wang, L. Deng, C. Feng, W. Tao, X. Xu, W. Cui, Biologically modified nanoparticles as theranostic bionanomaterials, Prog. Mater. Sci. (2020) 100768.

[31] J.L. Wu, F. Xu, S.M. Li, P.W. Ma, X.C. Zhang, Q.H. Liu, R.W. Fu, D.C. Wu, Porous polymers as multifunctional material platforms toward task-specific applications, Adv. Mater. 31 (2019), e1802922.

[32] Z. Yang, D. Gao, X. Guo, L. Jin, J. Zheng, Y. Wang, S. Chen, X. Zheng, L. Zeng, M. Guo, X. Zhang, Z. Tian, Fighting immune cold and reprogramming immunosuppressive tumor microenvironment with red blood cell membrane-camouflaged nanobullets, ACS Nano 14 (2020) 17442–17457.

[33] T. Liu, W. Liu, M. Zhang, W. Yu, F. Gao, C. Li, S.B. Wang, J. Feng, X.Z. Zhang, Ferrous-supply-regeneration nanoengineering for cancer-cell-specific ferroptosis in combination with imaging-guided photodynamic therapy, ACS Nano 12 (2018) 12181–12192.

[34] M.T. Zhao, K. Yuan, Y. Wang, G.D. Li, J. Guo, L. Gu, W.P. Hu, H.J. Zhao, Z.Y. Tang, Metal-organic frameworks as selectivity regulators for hydrogenation reactions, Nature 539 (2016) 76–80.

[35] H.Q. Zheng, Y.N. Zhang, L.F. Liu, W. Wan, P. Guo, A.M. Nystrom, X.D. Zou, One-pot synthesis of metal organic frameworks with encapsulated target molecules and their applications for controlled drug delivery, J. Am. Chem. Soc. 138 (2016) 962–968.

[36] G. Lu, S. Li, Z. Guo, O.K. Farha, B.G. Hauser, X. Qi, Y. Wang, X. Wang, S. Han, X. Liu, J.S. DuChene, H. Zhang, Q. Zhang, X. Chen, J. Ma, S.C. Loo, W.D. Wei, Y. Yang, J.T. Hupp, F. Huo, Imparting functionality to a metal-organic framework material by controlled nanoparticle encapsulation, Nat. Chem. 4 (2012) 310–316.

[37] C. Serre, F. Millange, C. Thouvenot, M. Nogues, G. Marsolier, D. Louer, G. Ferey, Very large breathing effect in the first nanoporous chromium(III)-based solids: MIL-53 or Cr-III(OH)·x·H2Oy, J. Am. Chem. Soc. 124 (2002) 13519–13526.

[38] F. Lyu, Y. Zhang, R.N. Zare, J. Ge, Z. Liu, One-pot synthesis of protein-embedded metal-organic frameworks with enhanced biological activities, Nano Lett. 14 (2014) 5761–5765.

[39] P. Horcajada, C. Serre, G. Maurin, N.A. Ramsahye, F. Balas, M. Vallet-Regi, M. Sebban, F. Taulelle, G. Ferey, Flexible porous metal-organic frameworks for a controlled drug delivery, J. Am. Chem. Soc. 130 (2008) 6774–6780.

[40] E. Ben-Akiva, R.A. Meyer, H.Z. Yu, J.T. Smith, D.M. Pardoll, J.J. Green, Biomimetic anisotropic polymeric nanoparticles coated with red blood cell membranes for enhanced circulation and toxin removal, Sci. Adv. 6 (2020), eaay9035.

[41] R. Guo, Y. Tian, Y. Wang, W. Yang, Near-infrared laser-triggered nitric oxide nanogenerators for the reversal of multidrug resistance in cancer, Adv. Funct. Mater. 27 (2017) 1606398.

[42] J.J. Liu, M. Wu, Y.T. Pan, Y.K. Duan, Z.L. Dong, Y. Chao, Z. Liu, B. Liu, Biodegradable nanoscale coordination polymers for targeted tumor combination therapy with oxidative stress amplification, Adv. Funct. Mater. 30 (2020) 1908865.

[43] Y. Liu, W.Y. Zhen, L.H. Jin, S.T. Zhang, G.Y. Sun, T.Q. Zhang, X. Xu, S.Y. Song, Y. H. Wang, J.H. Liu, H.J. Zhang, All-in-one theranostic nanoagent with enhanced reactive oxygen species generation and modulating tumor microenvironment ability for effective tumor eradication, ACS Nano 12 (2018) 4886–4893.

[44] X. Wan, H. Zhong, W. Pan, Y. Li, Y. Chen, N. Li, B. Tang, Programmed release of dihydroartemisinin for synergistic cancer therapy using a CaCO3 mineralized Metal-Organic Framework, Angew. Chem. Int. Ed. 58 (2019) 14134–14139.

[45] X.Z. Lian, Y.Y. Huang, Y.Y. Zhu, Y. Fang, R. Zhao, E. Joseph, J.L. Li, J.P. Pellois, H. C. Zhou, Enzyme-MOF nanoreactor activates nontoxic paracetamol for cancer therapy, Angew. Chem. Int. Ed. 57 (2018) 5725–5730.

[46] Q. Yin, J. Shen, Z. Zhang, H. Yu, Y. Li, Reversal of multidrug resistance by stimuli-responsive drug delivery systems for therapy of tumor, Adv. Drug Deliv. Rev. 65 (2013) 1699–1715.